Astron. Astrophys. 356, 287–300 (2000)

ASTRONOMY AND ASTROPHYSICS

The shock waves in decaying supersonic turbulence

M.D. Smith[1], **M.-M. Mac Low**[2,3], **and J.M. Zuev**[4]

[1] Armagh Observatory, College Hill, Armagh BT61 9DG, Northern Ireland
[2] Max-Planck-Institut für Astronomie, Königstuhl 17, 69117 Heidelberg, Germany
[3] Department of Astrophysics, American Museum of Natural History, 79th St. at Central Park West, New York, New York, 10024-5192, USA
[4] JILA, University of Colorado, Boulder, Campus Box 440, Boulder, CO 80309, USA
(mds@star.arm.ac.uk; mordecai@amnh.org; julia.zuev@colorado.edu)

Received 20 October 1999 / Accepted 25 January 2000

Abstract. We here analyse numerical simulations of supersonic, hypersonic and magnetohydrodynamic turbulence that is free to decay. Our goals are to understand the dynamics of the decay and the characteristic properties of the shock waves produced. This will be useful for interpretation of observations of both motions in molecular clouds and sources of non-thermal radiation.

We find that decaying hypersonic turbulence possesses an exponential tail of fast shocks and an exponential decay in time, i.e. the number of shocks is proportional to $t\ \exp(-ktv)$ for shock velocity jump v and mean initial wavenumber k. In contrast to the velocity gradients, the velocity Probability Distribution Function remains Gaussian with a more complex decay law.

The energy is dissipated not by fast shocks but by a large number of low Mach number shocks. The power loss peaks near a low-speed turn-over in an exponential distribution. An analytical extension of the mapping closure technique is able to predict the basic decay features. Our analytic description of the distribution of shock strengths should prove useful for direct modeling of observable emission. We note that an exponential distribution of shocks such as we find will, in general, generate very low excitation shock signatures.

Key words: hydrodynamics – shock waves – turbulence – ISM: clouds – ISM: kinematics and dynamics

1. Introduction

Many structures we observe in the Universe have been shaped by fluid turbulence. In astronomy, we often observe high speed turbulence driven by supersonic ordered motions such as jets, supernova shocks and stellar winds (e.g. Franco & Carraminana 1999). Hypersonic speeds, with Mach numbers above 10, are commonly encountered. Clearly, to understand the structure, we require a theory for supersonic turbulence. Here, we concentrate on decaying turbulence, such as could be expected in the wakes of bow shocks, in the lobes of radio galaxies or following explosive events. Two motivating questions are: how fast does supersonic turbulence decay when not continuously replenished and how can we distinguish decaying turbulence from other dynamical forms? The first question has been answered through recent numerical simulations described below. The answer to the second question is sought here. We look for a deep understanding of the dynamics and physics which control decaying supersonic turbulence. From this, and a following study of driven turbulence, we can derive the analytical characteristics and the observational signatures pertaining to supersonic turbulence. We caution that we specify to uniform three dimensional turbulence with an isothermal equation of state, an initially uniform magnetic field and periodic boundary conditions.

Numerical studies of decaying supersonic turbulence in three dimensions have revealed a power-law decay of the energy in time following a short low-loss period (Mac Low et al. 1998; Stone et al. 1998). Simulations of decaying subsonic and incompressible turbulence show similar temporal behaviour (e.g. Galtier et al. 1997), as discussed by Mac Low et al. (1999). In the numerical experiments, random Gaussian velocity fields were generated with small wavenumber disturbances. Magnetic fields were included of various strengths. Mac Low (1999) concluded that the decay is so rapid under all conditions that the motions we observe in molecular clouds must be continuously driven. In this work, we analyse the Mach 5 simulations from Mac Low et al. (1998) as well as a new Mach 50 simulation. The hypersonic run should best illustrate the mechanisms behind the development and evolution of the shock field, possibly revealing asymptotic solutions.

The major goal is to derive the spectrum of shocks (the Shock Probability Distribution Function) generated by turbulence. Shocks are often responsible for detailed bright features, such as filamentary and sheet structures, within which particles are highly excited. An example of a region which appears to contain a chaotic mixture of shocks, termed a 'Supersonic Turbulent Reactor' is the DR 21 molecular hydrogen outflow, driven by a collimated wind from a high mass young star (Smith et al. 1998). The shock spectrum is related to the molecular excitation, with weak shocks being responsible for rotational excitation and strong shocks for vibrational excitation.

Send offprint requests to: M.D. Smith

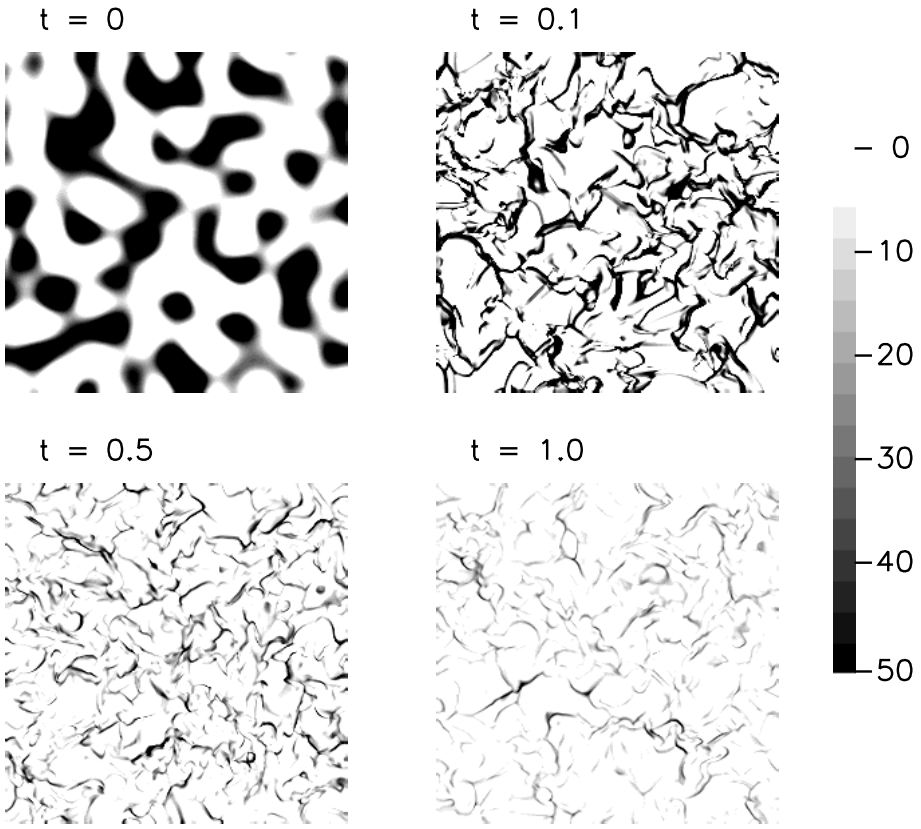

Fig. 1. Four stages in the early development of the shock field. The distribution of converging regions (i.e. the negative velocity divergence of the velocity field) is displayed here for a cross-sectional plane of the hydrodynamic M = 50 simulation. The displayed values are the numerical equivalents of the divergence (i.e. the sum of the velocity differences) at each grid location. In order of increasing time, the minimum divergence (maximum convergence) and the average divergence within converging regions only in the displayed cross-sections are: (-178.4, -46.6), (-441.9, -48.0), (-146.7, -13.74) and (-99.9, -7.3).

Previous studies of compressible turbulence have concentrated on the density and velocity structure of the cold gas rather than the shocks. Three dimensional subsonic and transonic simulations (e.g. Porter et al. 1994; Falgarone et al. 1994), two dimensional supersonic motions (Vázquez-Semadeni 1994) as well as three dimensional supersonic turbulence have been discussed (Vázquez-Semadeni et al. 1996; Padoan et al. 1998). One attempts to describe and fit the density and velocity structures observed in molecular clouds. This is often appropriate for the interpretation of clouds since, although the Mach number is still high, the shock speeds are too low to produce bright features. The simulations analysed here are also being interpreted by Mac Low & Ossenkopf (2000) in terms of density structure.

Despite a diversity of theory, and an increase in analytical knowledge, a succinct understanding of turbulence has not been attained (see Lesieur 1997). Therefore, we need not apologise for not fully interpreting the results for the supersonic case. We do not look for a Kolmogorov-inspired theory for two reasons. First, fully developed turbulence becomes increasingly non-Gaussian towards small scales. These intermittency effects dominate the statistics of velocity jumps in supersonic turbulence. Second: the strong compressibility implies that a wavenumber analysis is irrelevant since the energy spectrum of a shock or of a system of shocks is simply k^{-2} (e.g. Gotoh & Kraichnan 1993). Note that the Kolmogorov-like spectra found by Porter et al. (1994) appeared at late times when the flow is clearly subsonic (and also note that even the initial RMS Mach number was only unity, which rather stretches the definition of supersonic turbulence).

We attempt here to construct a physical model to describe the non-Gaussian Probability Density Functions (PDFs) for the shock waves. We adapt the mapping closure analysis, as applied to Navier-Stokes (incompressible) and Burgers (one dimensional and pressure free) turbulence (Kraichnan 1990), to compressible turbulence. Phenomenological approaches, such as multifractal models or the log-normal model, are avoided since they have limited connection to the underlying physical mechanisms. In contrast, mapping closure follows the stretching and squeezing of the fluid, and the competition between ram pressure, viscosity and advection determines the spectral form.

We study here compressible turbulence without gravity, self-gravity or thermal conduction. No physical viscosity is modelled, but numerical viscosity remains present, and an artificial viscosity determines the dissipation in regions of strong convergence. By strong convergence, we mean high negative divergence of the velocity field, which thus correspond to the shock zones as shown in Fig. 1. Periodic boundary conditions were chosen for the finite difference ZEUS code simulations, fully described by Mac Low et al. (1998).

The ZEUS code itself is a time-explicit second-order accurate finite difference code (Stone & Norman 1992a,b). It is ideal for problems involving supersonic flow and is versatile, robust and well-tested. Although higher order codes are potentially more accurate, the high speed of the algorithms means that

large problems can be solved at high resolution. This enables us to test for convergence of the energy dissipation rate (Mac Low et al. 1998), shock distributions (Sect. 2.4) and numerical viscosity (Sect. 2.6). Furthermore, the basic hydrocode results have been confirmed on solving the same problems with the contrasting method of smoothed particle hydrodynamics (Mac Low et al. 1998). The constrained transport algorithm (Evans & Hawley 1988) updated through use of the method of characteristics (Hawley & Stone 1995) is used to maintain a divergence-free magnetic field to machine accuracy and to properly upwind the advection.

We begin by discussing the method used to count shocks from grid-based simulations (Sects. 2.1-2.2). We then present the shock jump PDFs and provide analytical fits for the hypersonic M = 50 case (Sects. 2.3-2.5). The one-dimensional counting procedures are verified through a comparison with full three-dimensional integrations of the dissipated energy (Sect. 2.6). Supersonic hydrodynamic M = 5 (Sect. 3) and magnetohydrodynamic (Alfv́en numbers A = 1 and A = 5) simulations (Sect. 4) are then then likewise explored. Note the definition of the Alfvén Mach number $A = v_{\rm rms}/v_{\rm A}$, where $v_{\rm A}^2 = B^2/4\pi\rho$ where $v_{\rm rms}$ is the initial root mean square (RMS) velocity and $v_{\rm A}$ is the Alfvén speed. The evolution of the velocity PDFs are then presented and modelled (Sect. 5). Finally, we interpret the results in terms of the dynamical models (Sect. 6).

2. Hydrodynamic hypersonic turbulence

2.1. Model description

The example we explore in detail is the decay of hypersonic hydrodynamic turbulence (Fig. 1). The three dimensional numerical simulation on a $D^3 = 256^3$ grid with periodic boundary conditions began with a root mean square Mach number of M = 50. The initial density is uniform and the initial velocity perturbations were drawn from a Gaussian random field, as described by Mac Low et al. (1998). The power spectrum of the perturbations is flat and limited to the wavenumber range $1 < k < k_{max}$ with $k_{max} = 8$.

The simulations employ a box of length 2L (hence L is equivalent to 128 zones in this example) and a unit of speed, u. The gas is isothermal with a sound speed of $c_s = 0.1u$. Hence the sound crossing time is 20L/u. We take the time unit as τ = L/u. Thus a wave of Mach 50 would laterally cross the box in a time 0.4τ if unimpeded.

Cross-sections of the shock distribution are shown at four times in Fig. 1. We actually display a greyscale image, biased to the high-convergence regions. An evolution is hardly discernable in snapshots showing all converging regions equally shaded (as displayed in Fig. 1 of Mac Low et al. 1999).

2.2. Shock number distribution

Ideally, we would like to calculate the total surface area for each shock strength as a function of time. We introduce the shock number distribution function dN/dv, which is the number of shock elements per unit shock speed as a function of time and shock speed. A shock element is the surface area of a shock put into units of the grid cell area.

To simplify our numerical analysis, we calculate instead the one dimensional shock jump function. This is the number distribution of the total jump in speed across each converging region along a specific direction. This is written as dN/dv_j where v_j is the sum of the (negative) velocity gradients (i.e. $\Sigma\left[-\delta v_x\right]$ across a region being compressed in the x-direction). We employ the jump Mach number in the x-direction $\mathrm{M}_j = v_j/c_s$ rather than v_j since this is the parameter relevant to the dynamics. Thus, each bounded region of convergence in the x-direction counts as a single shock and the total jump in M_j across this region is taken as its strength.

Numerically, over the whole simulation grid (x,y,z), we calculate each shock jump through

$$M_j = \sum_{x=x_i}^{x=x_f} (\Delta v_x/c_s) \tag{1}$$

with the condition that $\Delta v_x < 0$ in the range $x_i \leq x < x_f$. This is then binned as a single shock element. The shock number distribution dN/dM_j is obviously dimensionless.

The 1D approach neglects both the shock angle and full shock strength. The distribution of shock jumps, however, is found by adding up an enormous number of contributions over the whole grid. This method has the advantage of being extremely robust, involving no model assumptions. To be a direct representation of the true shock strength function, however, it requires a few assumptions to be justified: (1) a one-dimensional shock jump is related to the actual shock speed, (2) not too many shocks are excluded because their surfaces are aligned with the chosen direction, (3) the shock velocities are distributed isotropically and (4) unsteepened compressional waves can be distinguished from true shocks.

First, we note that it is an extremely difficult task to calculate the actual shock speed for each shock. It is, however, unnecessary since the shock speed and one-dimensional shock jump are closely related statistically. We also take the number of zones at which compressive jumps are initiated as the number of shocks (where shocks are colliding, the method will be inaccurate). Assumption (3) will not hold for the magnetohydrodynamic turbulence which has a defined direction. In these cases, the jump distributions must be calculated both parallel and transverse to the original magnetic field. Assumption (4) will not be made: we include all acoustic waves, but we have followed the width of the jumps and so can verify whether shocks or waves are being counted. This is important since broad compressional waves also dissipate energy and become increasingly significant, of course, as the high-speed shocks decay and the flow eventually becomes subsonic.

Many shock surfaces are distorted, occasionally bow-shaped. This does not negate our counting procedure provided the curvature is not too strong. Here the relevant lengths are the shock radius of curvature and the shock width. The latter is determined by our numerical method, involving von Neumann & Richtmyer (1950) artificial viscosity, which here constrains

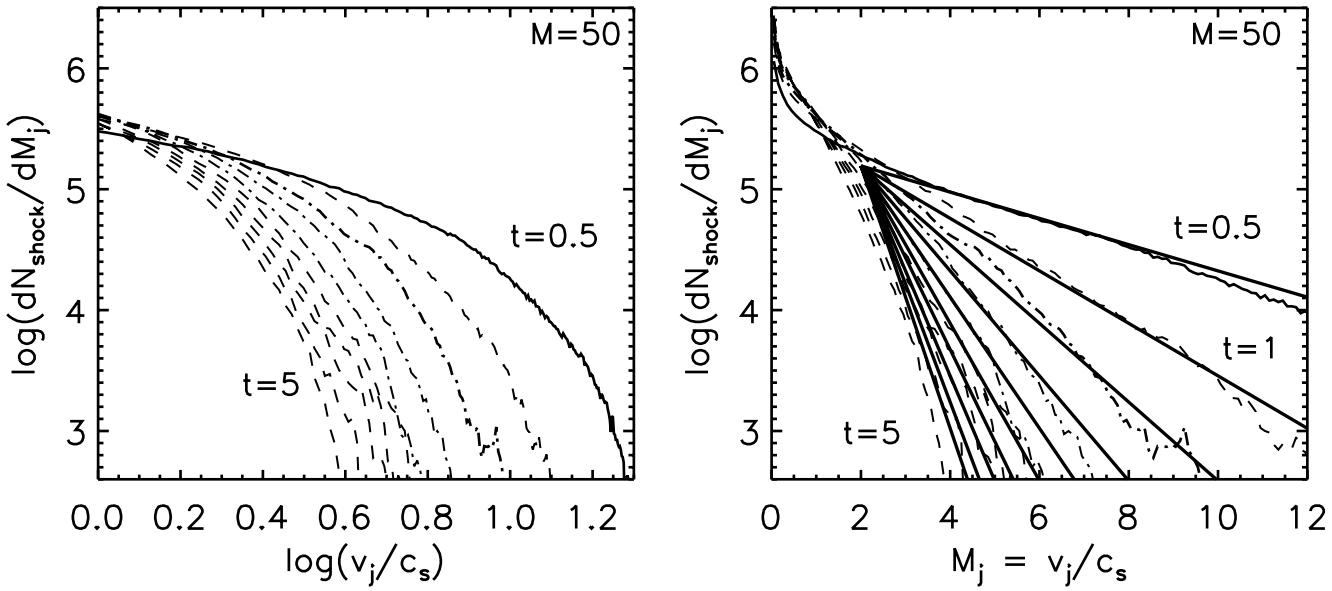

Fig. 2. The jump velocity distribution. Two representations of the number of compressive layers in the x-direction as a function of the total x-speed change across the layer at 10 equally-spaced times beginning at time $t = 0.5$ (solid line) and continuing, with a monotonic decay of the high-speed jumps, in time steps of 0.5. They demonstrate the decay and steepening and that (a) no power law can represent the behaviour at any stage, and (b) a series of exponentials of the form $\exp(-t(v_j - 2)/2)$ fit the high velocities well.

strong shocks to just a few zones. As seen from Fig. 1, we can confidently take one-dimensional cuts across the shock surfaces and equate the measured jump to the actual jump in speed of fluid elements to a good first approximation.

In Sect. 2.6, we check our method by demanding consistency with integrated quantities derived directly from the numerical simulations.

2.3. Hypersonic turbulence

The random Gaussian field rapidly transforms into a shock field in the Mach 50 case (Fig. 1). The shock steepening is reflected in the initial increase in the minimum value of the divergence (see the caption to Fig. 1). Note that the *average* value of the divergence does not change i.e. the total number of converging zones only falls from half to about one third, despite the steepening. The explanation is that the shocks have time to form in the strongly converging regions but the compression in most of the flow progresses slowly. After the time t = 0.1, the number of fast shocks decays and the average convergence decreases. The total number of zones with convergence, however, remains constant throughout. This fact, that the total shock surface area is roughly conserved, is verified in the following analysis.

The one-dimensional distribution of the number of shock jumps as a function of time is presented in Fig. 2 for the case with RMS Mach number M = 50. This demonstrates that the shock jump function both decays and steepens. One can contrast this to the decay of incompressible turbulence where the distribution function, as measured by wavenumber, maintains the canonical Kolmogorov power-law in the inertial range during the decay (Lesieur 1997). Here we remark that a power-law fit is impossible (Fig. 2a) but stress that this result applies only to the case at hand: *decaying* turbulence.

The jump distribution is very close to being exponential in both velocity and time. This remarkably simple conclusion is based on the good fits shown in Fig. 2b. Note that the pure exponential only applies to the medium and strong shock regime. To also account for the low Mach number regime, we fitted a further time dependence as shown in Fig. 3, yielding

$$\frac{dN}{dM_j} = 10^{5.72}\, t\, \exp(-M_j\, t/2.0) \tag{2}$$

in terms of the 1-D jump Mach number. Better fits can be obtained with a somewhat more complex time dependence. We find excellent fits for

$$\frac{dN}{dM_j} = 10^{5.79}\, t \exp\left[-\beta\, M_j\, t^{\alpha}\right] \tag{3}$$

with $\alpha \sim 0.88 \pm 0.03$ and $\beta \sim 0.52 \pm 0.03$. The values and errors are derived from parameter fitting of all the displayed curves to within a factor of ~ 1.5. We exclude in this process the phase where collisional equilibrium would not be expected: at early times and low Mach numbers $t\, M_j < 0.5$. Also, we exclude the jump speeds where the jump counts are low (shock numbers $dN/dM_j < 3000$).

2.4. Convergence and dependence on initial conditions

Resolution studies are essential to confirm numerical results. One hopes that the results demonstrate convergence. This is plausible for supersonic flow in which the decay does not depend on the details of the viscosity or the details of the shock transitions. This has been confirmed for the analysis of the total energy (Mac Low et al. 1998).

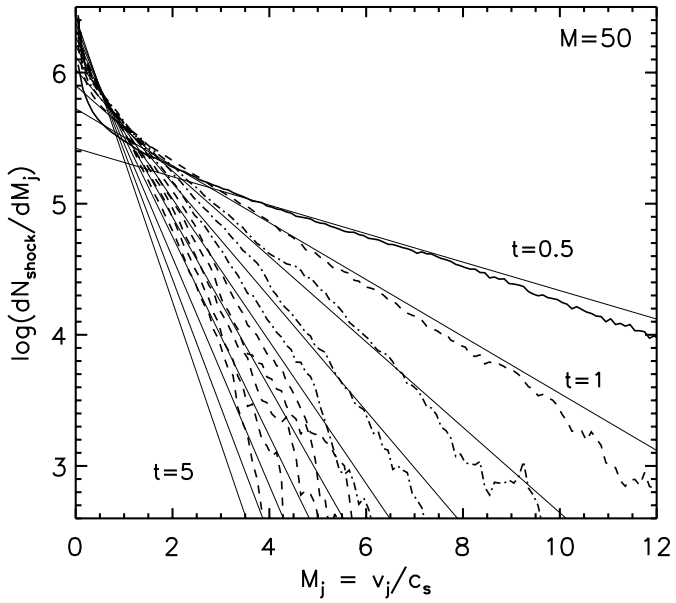

Fig. 3. The jump velocity distribution extracted from the M = 50 hydrodynamic simulation as a function of time, as in Fig. 2. The fitted function is $dN/dM_j = 10^{5.42}\, t \exp(-tM_j/2)$.

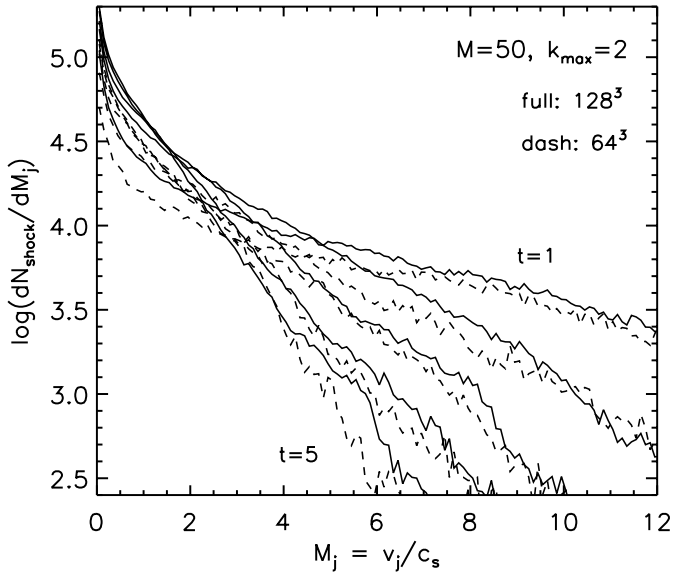

Fig. 4. The evolution of the jump velocity distribution at two resolutions for M = 50 hydrodynamic simulation with k_{max} = 2. The shock number for the 64^3 simulation has been multiplied by 4 to adjust for the larger zone sizes.

We compare available simulations for the hypersonic study with 64^3 and 128^3. We also set the initial wavenumber range to $k_{max} = 2$ and can thus examine the dependence on the chosen initial state.

The results at the two different resolutions are in quite good agreement, especially in the high Mach number regime (Fig. 4). The density of high Mach number shocks is quite low and they are well resolved. At low Mach numbers, the lower resolution simulation fails, of course, to capture the vast quantities of weak

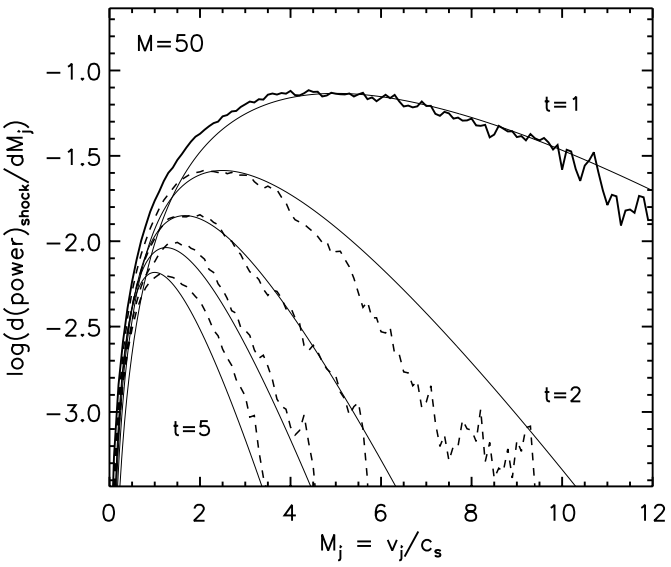

Fig. 5. The power dissipated as a function of the jump velocity. The power is displayed per unit M_j where $M_j = v_j/c_s$, and the data is extracted from the M = 50 hydrodynamic simulation for times t = 1,2,3,4 & 5. The fitted function is $d\dot{E}/dM_j = 0.016\, t\, M_j^{2.5} \exp(-tM_j/2)$.

compressional waves contained in the higher resolution example. It is to be expected that shock turbulence configurations get extremely complex on small scales, through the interactions which produce triple-point and slip-layer structures. To capture this structure requires adaptive grid codes. This does not mean, however, that the simulations are inaccurate for our purposes since energy dissipation is not controlled by the weak shocks until very late times, as verified in Fig. 5.

A similar formula for the shock jump function is found. The evolution, however, is three times slower. We show in Fig. 6 the model fit

$$\frac{dN}{dM_j} = 10^{4.23}\, t\, \exp(-M_j\, t/6.0). \tag{4}$$

This suggests that the rate of decay is proportional to the initial mean wavenumber of the wave distribution. The decay $k_{max} = 2$ simulation is a factor of three slower than in the $k_{max} = 8$ simulation. The mean wavenumber of the two simulations are $k_m = 1.5$ and 4.5, with flat initial energy distributions. Hence, given that $M_j = v_x/c_s$ and t is in units of $L/10c_s$, the shock numbers are approximately $\propto t \exp(-k_o t\, v_j)$ where $k_o \sim 1.1\, k_m$. The dependence on the initial mean wavenumber is expected since the box size should not influence the decay rate if we are indeed, as we wish, following the unbounded decay.

Note that two parameter fitting, as above, in this case yields

$$\frac{dN}{dM_j} = 10^{4.23}\, t \exp\left[-\beta\, M_j\, t^{\alpha}\right] \tag{5}$$

with $\alpha \sim 1.02 \pm 0.03$ and $\beta \sim 0.168 \pm 0.008$.

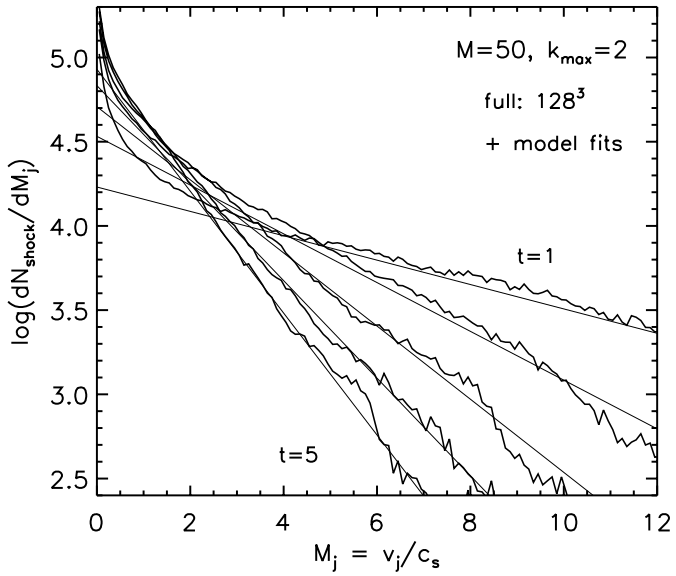

Fig. 6. The jump velocity distribution extracted from the 128^3 M = 50 hydrodynamic simulation with k_{max} = 2 as a function of time. The fitted function is $dN/dM_j = 10^{3.93}\, t \exp(-tM_j/6)$.

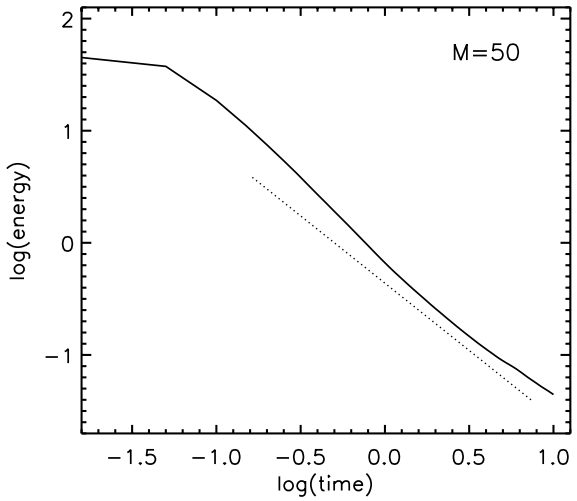

Fig. 7. The total energy as a function of time (full line) from data extracted from the M = 50 hydrodynamic simulation. For comparison, the dashed line is a power law with exponent -1.5.

2.5. Shock power distribution

How is the spectrum of shock jumps related to the decay of energy? Here we show that the energy dissipation in the fast shocks is directly correlated with their number which is decreasing exponentially. Furthermore, the weakest shocks, which merge into an area of 'compressional waves', are ineffective in the overall dissipation. The result is that the moderately-supersonic part of the turbulence rapidly becomes and remains responsible for the energy dissipation for an extended time.

The shock power distribution function is here defined as the energy dissipated per unit time per unit jump speed v_j as a function of jump speed. Here again we employ the uni-directional jump Mach number M_j. We actually calculate the energy dissipated by artificial viscosity acting along a specific direction within the shocks as defined by convergence along this direction. Hence we anticipate that in isotropic turbulence one third of the full loss will be obtained. The relative contributions of artificial and numerical viscosity, which also confirms the method employed here, are discussed in Sect. 2.5.

The jump *number* distribution includes a high proportion of very weak compressional waves that dissipate little energy. The one-dimensional shock power distribution, $d\dot{E}/dM_j$, shown in Fig. 5, illustrates this. The functional fit is guided by the above shock number distributions, which we would expect to remain accurate for the high Mach number jumps. We display the fit to:

$$\frac{d\dot{E}}{dM_j} = 0.016\, M_j^{2.5}\, t\, \exp(-k\, M_j\, t) \tag{6}$$

with k = 0.5, which is again remarkably accurate given the lack of adjustable parameters. Hence $d\dot{E}/dM_j \propto M_j^{2.5} d\dot{N}/dM_j$. Note that the energy dissipated across an isothermal steady shock of Mach number M and pre-shock density ρ is $\dot{E}_s$ = (ρc_s^3/2) M^3(1 - 1/M^2) and that the jump in Mach number is M_J = M(1 - 1/M^2). This yields

$$\dot{E}_s = 0.5\, \rho c_s^3\, M_J^3 \left[1 + \frac{\sqrt{(1 + 4/M_J^2)} - 1}{2}\right]. \tag{7}$$

Therefore, the numerical result suggests a (statistical) inverse correlation between density and shock strength.

Note that Eq. 6 yields $\dot{E} \propto t^{-2.5}$ (on integrating over M_j and substituting the variable $w = M_j t$) Thus, one obtains a power-law decay in total energy of the form E $\propto$ $t^{-1.5}$. This behaviour of the total energy decay and the energy dissipation rate, is indeed found in the simulations, as shown in Fig. 7. Hence the results are fully consistent with the simple fits. Note that the energy decay deviates from a pure power law: there is an early transition phase between times t = 0.1 - 0.5 during which the decay is more rapid (Fig. 7). This was not found in simulations of moderate Mach number supersonic turbulence (Mac Low et al. 1998) but appears here and also in simulations in which the supersonic turbulence is initially driven (Mac Low 1999).

2.6. Shock power and artificial viscosity

In order to check the approximations described in Sect. 2.2, we analyse how the energy dissipated due to artificial viscosity varies over time and with different parameters of the model. For non-driven, or freely decaying runs, the following equation is taken as a basic:

$$\frac{dE}{dt} = -(H_\nu + H_{\rm numerical}), \tag{8}$$

where H_ν and $H_{numerical}$ are energy dissipation rates due to artificial viscosity and numerical viscosity respectively.

We follow Stone & Norman (1992) Eqs. (32)-(34), (134) in computing H_ν. The first step in computing derivatives is to realize that artificial viscosity operates on compression only, so

points with positive derivatives in each direction are set to zero:

$$\partial v1_{i,j,k} = \begin{cases} 0 & \text{if } (v1_{i+1,j,k} - v1_{i,j,k}) > 0 \\ v1_{i+1,j,k} - v1_{i,j,k} & \text{otherwise.} \end{cases} \tag{9}$$

Then scalar artificial pressures q_i in all 3 directions are computed, with the uniform mesh (Δx):

$$q_i = l^2 \rho \left(\frac{\partial v_i}{\partial x_i} \right)^2 = \left[\frac{l}{\Delta x} \right]^2 \rho (\partial v_i)^2 \tag{10}$$

where $(l/\Delta x)^2$ is a dimensionless constant which measures the number of zones over which the artificial viscosity will spread a shock and was chosen to be 2 in these simulations. Then we calculate the artificial viscosity tensor h_ν:

$$\overleftrightarrow{h_\nu} = -\overleftrightarrow{\nabla v} : \overleftrightarrow{Q} = (-1) \left[\frac{\partial v1}{\partial x1} q1 + \frac{\partial v2}{\partial x2} q2 + \frac{\partial v3}{\partial x3} q3 \right] \tag{11}$$

and compute the artificial viscosity dissipation rate for the entire cube at each particular time dump as

$$H_\nu = \int \overleftrightarrow{h_\nu} \, dx^3 \sim \sum_{ijk} (h_{\nu,ijk}) \delta x^3. \tag{12}$$

To understand the convergence properties of the energy dissipation rate, we performed a resolution study for resolutions of 64^3, 128^3, and 256^3 zones for both hydrodynamic and MHD models. Fig. 8 shows that the energy dissipation rate H_ν has converged to better than 25% moving from the 128^3 to the 256^3 models.

Now let us examine the fraction of the total kinetic energy lost to dissipation in shocks due to artificial viscosity $R = H_\nu/(dE/dt)$. We avoid taking this ratio locally in time as variations of H_ν in time around the average lead to spurious results. A more robust way to compute this ratio is to integrate over the entire curve, thus averaging over the variations in H_ν by computing

$$R = \frac{\int H dt}{E_k(t_f) - E_k(t_0)}. \tag{13}$$

Table 1 shows these ratios for a set of models with $M = 5$ and $k_{max} = 8$. The table indicates that the energy dissipation ratio R has converged to a few percent in the hydrodynamic case at the resolution of 128^3, and even in the MHD case is converged to better than 3% at 256^3.

We find that the fraction of energy lost in shocks to artificial viscosity doubles when we go from MHD to hydrodynamic models. Mac Low et al. (1998) speculated that runs with magnetic fields dissipating much of their energy via short-wavelength MHD waves. The factor of two difference in the dissipation rate due to artificial viscosity from hydrodynamic to MHD runs gives further evidence for this dissipation mechanism. This behavior appears well-converged, as discussed above.

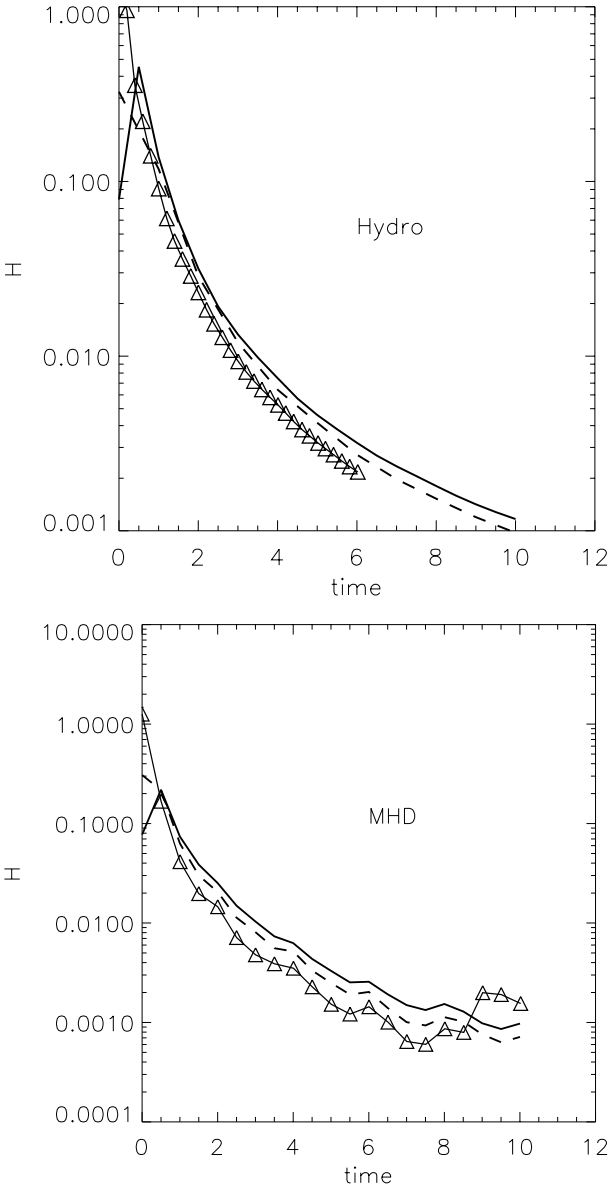

Fig. 8. Resolution study for 3D models – Energy dissipation rate due to artificial viscosity versus time. Top graph: model B (64^3, triangle), model C (128^3, dashed line), and model D (256^3, solid line). Bottom graph: model N (64^3, triangle), model P (128^3, dashed line), and model Q (256^3, solid line). For hydrodynamic models we observe that the energy dissipation rate H_ν has converged to better than 35% moving from 64^3 to the 128^3 models, and to better than 25% moving from the 128^3 to the 256^3 models. These values are 37% and 23% for the MHD models. Thus, energy dissipation rate due to artificial viscosity converges as we go to finer grids.

3. Supersonic turbulence: M = 5

Moderate-speed hydrodynamic turbulence has been discussed by Mac Low et al. (1998). They also found that the kinetic energy decreases with time as a power law, but with a shallower exponent. For the M=5 study (Model C) they recovered a E $\propto t^{-1.0}$ law.

Comparison of Ratios								
run	B	C	D	N	P	Q	J	L
grid	64^3	128^3	256^3	64^3	128^3	256^3	64^3	256^3
physics	Hydro	Hydro	Hydro	MHD	MHD	MHD	MHD	MHD
A	∞	∞	∞	1	1	1	5	5
R	0.62	0.68	0.68	0.38	0.36	0.35	0.59	0.49

Table 1. The fraction of the energy dissipated through artificial viscosity for models of supersonic turbulence. Ratio R is defined by Eq. (13). Model labels correspond to those of Table 1 of Mac Low et al. (1998). A is the RMS Alfvén Mach number.

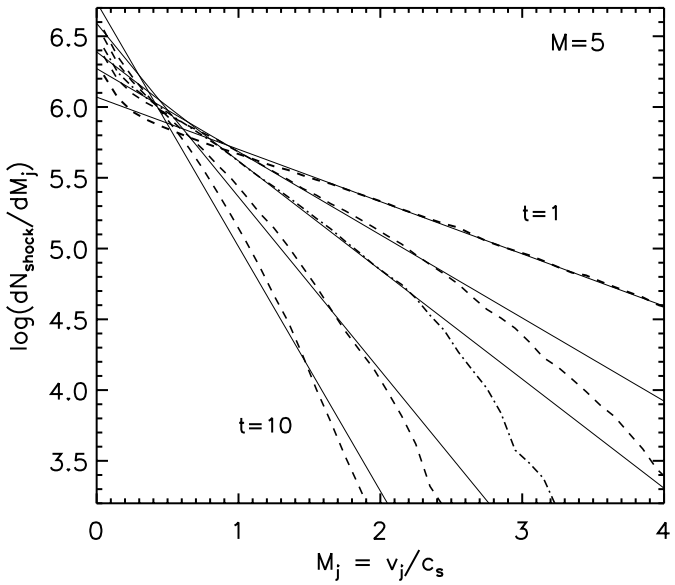

Fig. 9. The jump velocity distribution extracted from the M = 5 hydrodynamic simulation (Mac Low et al. 1998) as a function of time. The fitted function is exponential in velocity but more complicated in time (see text) ($\alpha = 0.67$ and $\beta = 0.85$ displayed). The time sequence shown is t = 1,2,3,5 and 10.

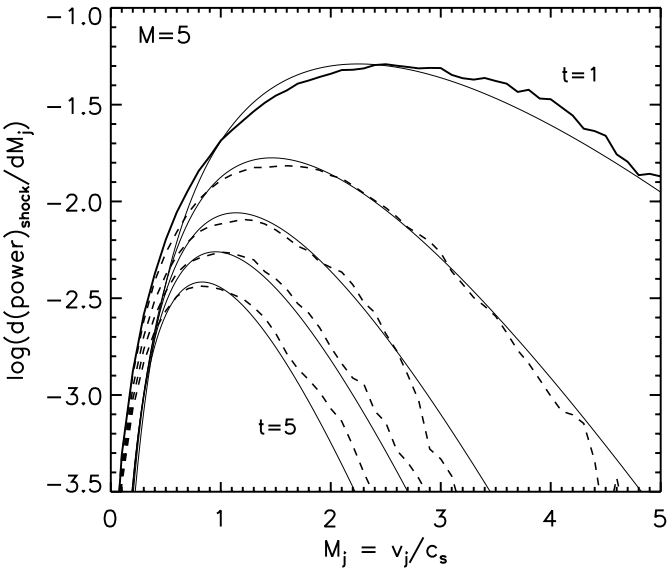

Fig. 10. The power dissipated as a function of the jump velocity. The power is displayed per unit M_j where $M_j = v_j/c_s$, and the data is extracted from the M = 5 hydrodynamic simulation for times t = 1,2,3,4 & 5. The fitted function, given in the text, takes $\alpha = 0.62$ and $\beta = 1.6$.

The shock jump distribution for M = 5 is shown in Fig. 9. Exponential velocity distributions are again found even though the range in Mach numbers over which we could expect a specific law is rather narrow ($M_j \sim 1 - 3$). Pure exponential time fits, however, are not accurate. We display a suitable fit, of the form

$$\frac{dN}{dM_j} = 10^{6.07}\, t^{\alpha} \exp(-\beta\, M_j t^{\alpha}) \tag{14}$$

with $\alpha \sim 0.67 \pm 0.05$ and $\beta \sim 0.85 \pm 0.1$. The corresponding shock power distribution is shown in Fig. 10 along with a best-fit family of curves calculated from

$$\frac{d\dot{E}}{dM_j} = 0.10\, M_j^{3.6}\, t^{\alpha} \exp(-\beta\, M_j t^{\alpha}) \tag{15}$$

with $\alpha = 0.62 \pm 0.04$ and $\beta = 1.6 \pm 0.1$.Hence, an exponential velocity distribution is maintained. The decay, however, is slightly slower. Integrating over M_j, yields $E \propto t^{-1.00}$.

Integrating over M_j, with the limits of integration from 0 to ∞ (to account for all the jumps), and with the substitution $x = Mt^{\alpha}$, we observe that the integral becomes time-independent. Thus, integration of Eq. 15 over M_j yields $dE/dt \propto t^{-2.23}$. This yields $dE/dt \propto t^{-1.23}$, which is quite close to the $E \propto t^{-1}$ law found by Mac Low et al. (1998).

Now we want to compare how the two quantities vary with time: dE/dt from Eq. 15 and the energy dissipation rate due to artificial viscosity H_ν, derived using the algorithm discussed in Sect. 2.6. Fig. 11 shows that the two methods indeed agree. Thus, the shock power distribution method (Sect. 2.6) confirms that the statistical approach works with power calculations for each 1D converging region.

4. MHD turbulence: M = 5, A = 1 and 5

An analysis of simulations of MHD turbulence allows us to determine which wave modes are involved. The time dependence of the kinetic energy of freely decaying MHD turbulence has been discussed by Mac Low et al. (1998). Remarkably, the kinetic energy also decreases with time as a power law, although with only a slightly shallower exponent than the equivalent hydrodynamic simulation. We consider here the high-field example in which the initial RMS Mach number M = 5 and the initial

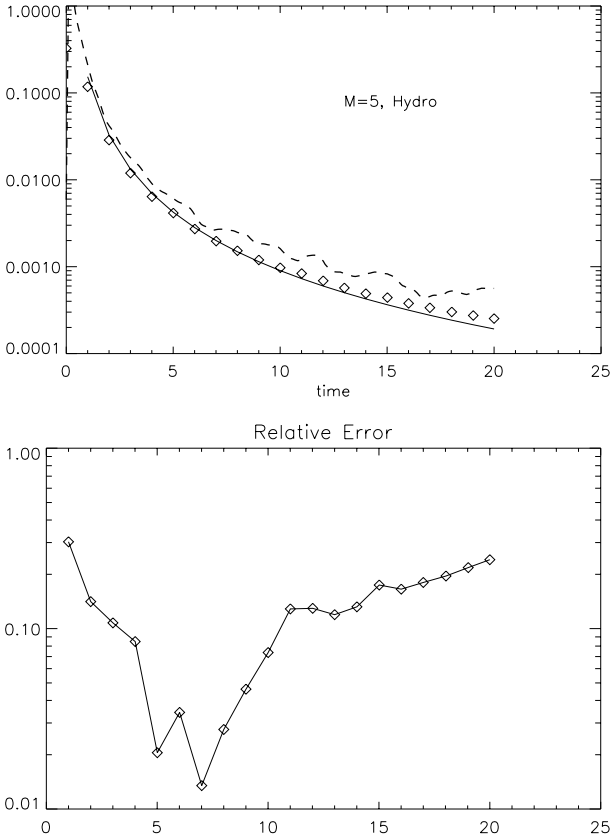

Fig. 11. Top: dE/dt versus time - the graph presents H_ν for model C (grid 128, M=5, hydrodynamic) for 21 time dumps (rhombs), and integral of Eq. (8) over dM_j (solid line). Both are energy dissipation rates due to artificial viscosity. We see a close fit of the methods. For comparison, dashed line represents total kinetic energy changes dE/dt directly from the numerical simulation output. Bottom: the absolute value of the relative error between H_ν and integrated Eq. (15).

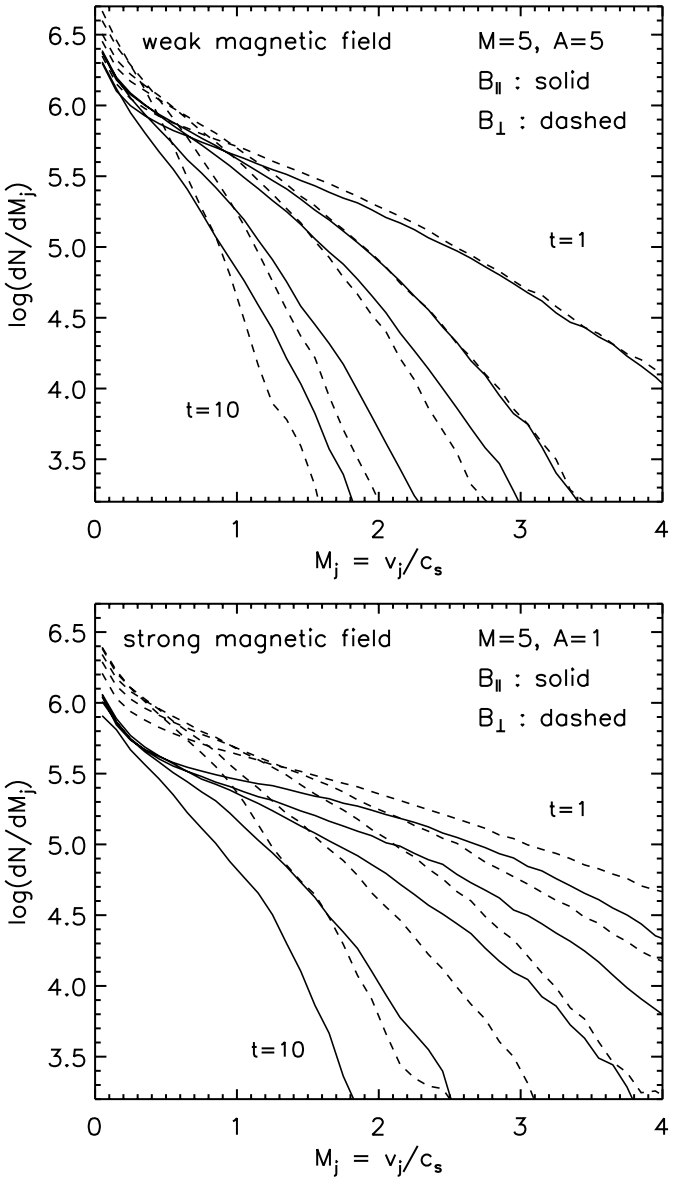

Fig. 12. The jump velocity distribution extracted from the M = 5 low magnetic field (A = 5) and high field (A = 1) MHD 256^3 simulations (Mac Low et al. 1998) as a function of time. The 5 times shown are t = 1,2,3,6 and 10. The two curves shown for each time are the velocity jumps transverse to the field (dashed) and parallel to the field (solid lines). The fitted exponentials are described in the text.

RMS Alfvén number A is unity and the low-field equivalent with A = 5. Mac Low et al. recovered: E $\propto t^{-0.87}$. (at the highest resolution of 256^3) for the high field case.

The initial field configuration is simply a uniform field aligned with the z-axis. Thus the imposed velocity field controls the turbulent energy input, and some energy is subsequently transferred into magnetic waves. We impose no turbulent diffusion here: magnetic energy may, however, still be lost through numerical diffusion or MHD wave processes.

The jump number distribution function for these simulation (Fig. 12) possesses exponential velocity distributions over a range in M_j. The displayed fit to the high field case (Fig. 13) is

$$\frac{dN}{dM_j} = 10^{5.94}\, t^{\alpha} \exp(-\beta\, M_j t^{\alpha}). \qquad (16)$$

where $\alpha \sim 0.66 \pm 0.03$ and $\beta \sim 0.62 \pm 0.03$. For the A = 5 case, $\alpha \sim 0.57 \pm 0.03$ and $\beta \sim 1.01 \pm 0.05$.

This analysis indicates that (1) supersonic MHD turbulence is, *mathematically* at least, no different from hydrodynamic turbulence in that the shock distribution is exponential and (2) the time dependencies are also similar to the hydrodynamic M = 5 case. From Fig. 12, we conclude (1) that the distribution of high speed shocks remains unchanged and isotropic in the low-field case, (2) the distribution of transverse waves is somewhat faster to decay when a weak field is present, whereas in the strong field case (3) the high speed transverse waves survive significantly longer from the outset and (4) the whole spectrum of parallel waves is suppressed by a factor ~ 2.

The velocity jump distributions plotted here are a combination of shocks and waves. Due to the high Alfvén speed, the shocks are predominantly slow shocks in the A = 1 case. These shocks can propagate with wave vectors in all directions ex-

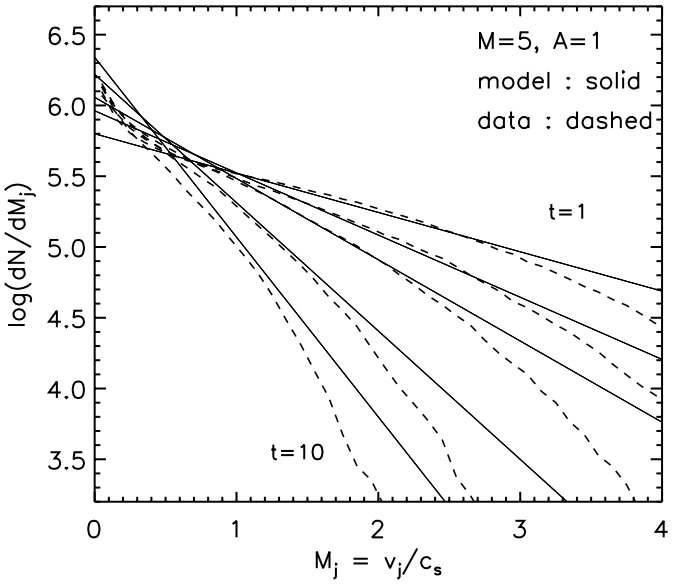

Fig. 13. Exponential fits to the jump velocity distributions for the high magnetic field (M = 5, A = 1) MHD 256^3 simulation. A mean value for the number of shocks in each direction has been taken. The 5 times shown are t = 1,2,3,6 and 10. The fitted exponentials are described in the text with $\alpha = 0.66$ and $\beta = 0.62$.

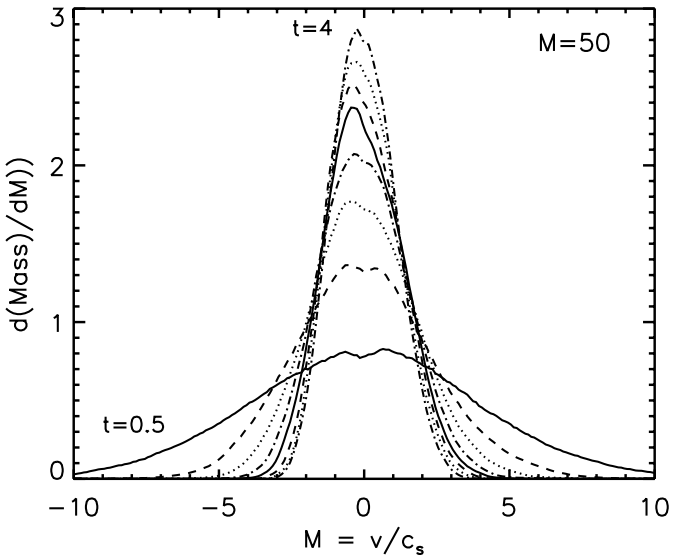

Fig. 14. The decay of the PDF for the M=50 simulation. The distributions are shown for the 8 equal time steps from 0.5 to 4

cept precisely transverse to the field. Their propagation speeds are relatively slow since the (initially-uniform) Alfvén speed is 5 times the sound speed), and therefore their energy may be transferred into faster waves via the turbulence raised in the magnetic field. In any case, it appears from Fig. 12 that about two-thirds of the compressional wave/shock energy is in transverse compression modes for the case A = 1. The waves in this case, as measured here by regions of convergence along the axes, are fast magnetosonic waves (close to compressional Alfvén waves). The proportion of each can be estimated from

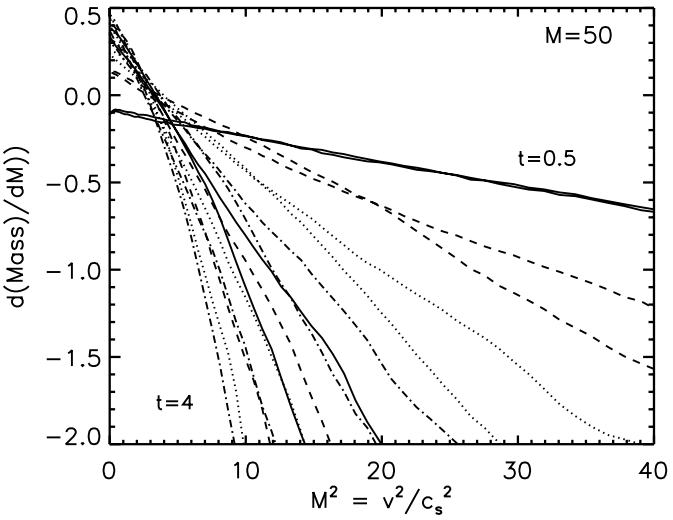

Fig. 15. A log-v^2 display of the decay of the PDF for the M=50 simulation demonstrates the Gaussian nature of the PDFs. The distributions for positive and negative absolute speeds are shown for the 8 equal time steps from 0.5 to 4, in descending order.

the simulations by calculating the jump widths (in practice, we here place the extra requirement that the one-dimensional jump across each individual zone exceeds $0.2\,c_s$, in order to distinguish the shocks from the waves). We then find that at M_j = 1, just over half the jumps are slow shocks (with an average resolution of ~ 3.0 and 3.3 zones transverse and parallel, respectively), while for $M_j > 4$, 76% of the 'jumps' are actually waves (an average of ~ 6.0 and 7.7 zones in each converging region). This contrasts with the hydrodynamic simulations where, quite uniformly, well over 90% of the jumps are indeed narrow shocks, resolved only by the artificial viscosity. These are of course estimates which ignore the possibility that many flow regions may be quite complex combinations of waves and shocks.

An explanation of why such different types of turbulence decay in the same functional manner is offered in Sect. 6.5.

5. The probability distribution functions

A traditional aid to understanding numerically-created turbulence is the probability distribution function (PDF) of the velocities. Here, we determine the one-dimensional Mass Distribution Function by calculating the mass per unit Mach number interval of the motion in the x-direction. Note all zones contribute here, whether in the shocks or not.

We recover Gaussian distributions in the velocity, as apparent in Fig. 14. This is clearly displayed on a Mass-log(M^2) plot for the high-speed wings (Fig. 15) where a Gaussian would generate a linear relationship. Note that each time step produces two lines, one for positive and one for negative absolute velocities. At early times, the imposed symmetry is still dominant but later on, small asymmetries become more apparent. To estimate the time dependence we have taken the mean mass fraction of each pair, on defining the initial mass density to be unity (i.e. a unit

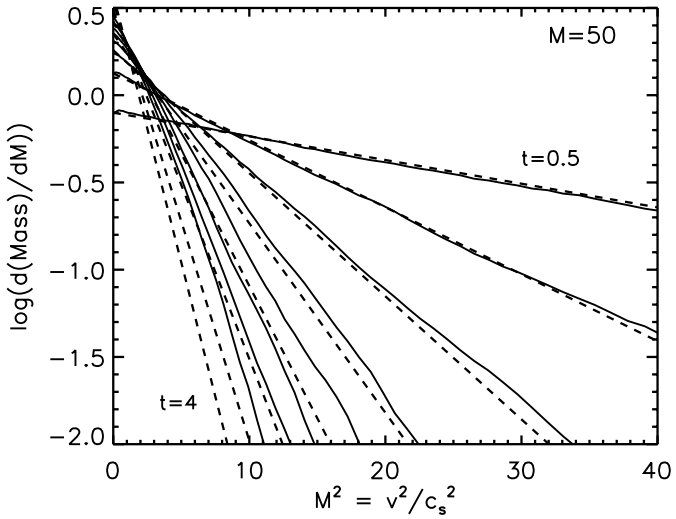

Fig. 16. Fits (dashed lines) to the decay of the PDF for the M=50 simulation. The mean distributions (full lines) are shown for the 8 equal time steps from 0.5 to 4. The model fits are given by Eq. 17, which is tailored so that the total mass in the box is conserved.

mass is initially contained in a box of size L^3) and found that a fit of the form

$$\frac{d(mass)}{dM} = 1.6\, t^{0.75} \exp(-0.088\, M^2 t^{1.5}) \tag{17}$$

is reasonable (Fig. 16). Interestingly, the decay in time of the PDF is not exponential. It is a faster decay law than for the shocks. This is inherent to the nature of decaying turbulence: in the beginning, closely-following shocks accelerate the fluid to high speeds. At late times, the fast shocks are quite evenly spread out and do not combine to produce high acceleration.

6. Interpretation of shock number distribution

6.1. The mapping closure method

A satisfying understanding of turbulence has been elusive. One can hope that supersonic turbulence may possess some simplifying aspects. We have thus devoted much time trying to interpret the above shock distributions of decaying turbulence. In this section, we first relate the numerical simulations to theoretical models which have predicted exponential velocity gradient PDFs for other forms of turbulence. We then interpret the evolution of the shock PDFs with an extension of these models utilising the ballistic (ram pressure) principles behind hypersonic turbulence.

We require a model based on local interaction in physical space in order to model shock interactions. We adapt the heuristic 'mapping closure' model in the form presented by Kraichnan (1990), in which analytical approximations were used to describe the evolution of Burgers turbulence. First, the initial competition between the squeezing and viscous processes is followed. An assumed Gaussian reference field is distorted nonlinearly in time into a dynamically evolving non-Gaussian field. Velocity amplitude and physical space are remapped by choosing transformations of particular forms. The PDF of a two-point velocity difference changes smoothly from Gaussian at very large separations (relating independent points) to some function ξ at small distances. The mapping functions are then determined by matching the evolution equations with the dynamical equations. The closure is obtained by limiting the form of the distortions to locally determined transformations.

The model for Burgers turbulence provides our inspiration since, in the hypersonic flow simulations of isothermal gas, thermal pressure is only significant within the thin shock fronts. Furthermore, individual shock structures are predominantly one-dimensional. Care must be exercised, however, since regions of vorticity are created behind curved shocks which are absent in the one-dimensional Burgers turbulence.

6.2. Background formulation

We assume a known *reference field* for the initial velocity $\mathbf{u_o}(\mathbf{z})$ as a function of a *reference* coordinate system $\mathbf{z}$ (Gotoh & Kraichnan 1993). The 'surrogate' velocity field is $\mathbf{u}(\mathbf{x}, t)$ and is related to $\mathbf{u_o}$ and the reference coordinates by vector and tensor mapping functions X and J:

$$u_i = X_i(\mathbf{u_o}, t), \tag{18}$$

$$\partial z_i/\partial x_j = J_{ij}(\mathbf{u_o}, \xi_\mathbf{o}, t) \tag{19}$$

where reference velocity gradients are $\xi_{ij,o} = \partial u_{i,o}/\partial z_j$ and velocity gradients are $\xi_{ij} = \partial u_i/\partial x_j$. The goal is to find the distortions described by X and J for which the surrogate velocity field is a valid approximation to the velocity field as given by the equations of motion. The above transformations, however, constrain the allowed forms of higher order statistics and, hence, neglect some physics which affect the long-term evolution (Gotoh & Kraichnan 1993).

Mapping closure also assumes that the velocity PDFs $P(u_o)$ and $P(u)$ are related to multivariate-Gaussians through prescribed forms. The justification is simply the statistical mechanics argument, as applied to particle speeds in equilibrium thermodynamics. The velocity gradient PDF is written as $Q(\xi, t)$ with u and ξ taken to be statistically independent.

For convenience, we concentrate on the component of the velocity, u_i, in the x_i direction. We rewrite the decay of velocity amplitudes in the simpler form

$$u_i = X_i(\mathbf{u_o}, t) = r_i(t)\, u_{i,o}(z_i), \tag{20}$$

and the velocity gradients then map through

$$\frac{\partial u_i}{\partial x_i} = \xi_{ii} = r_i(t)\xi_{ii,o} J_{ii}(\mathbf{u_o}, \xi_\mathbf{o}, t) = Y_{ii}(\xi_o, t), \tag{21}$$

so defining Y. The velocity gradient PDF, which contains the shock PDF, can now be written

$$Q(\xi_{ii}) = Q_o(\xi_{ii,o}) \left[\frac{\xi_{ii}}{\xi_{ii,o}}\right]^{-1} \frac{N}{J_{ii}} \tag{22}$$

where $N(t)$ normalises the PDF. This is the framework in which we can discuss the statistical evolution of velocity gradients.

6.3. Dynamical input

The momentum equations being solved, with the pressure gradients neglected, are $Du_i/Dt = (1/\rho)(\partial/\partial x_j)\mu\sigma_{i,j}$ where $Du_i/Dt = \partial u_i/\partial t + u_j \partial u_i/\partial x_j$, $\sigma_{i,j}$ is the stress tensor and μ is the viscosity. Differentiation yields the velocity gradient equation:

$$\frac{D\xi_{ii}}{Dt} + \xi_{ik}\xi_{ki} = -\frac{1}{\rho}\frac{\partial}{\partial x_i}\frac{\partial}{\partial x_j}(\mu\sigma_{i,j}) \tag{23}$$

where the usual summation rule applies to j and k (but i is a chosen direction).

To continue, we can derive the evolution of the functions J, by equating $Q(\xi, t)$ as derived from these equations (yielding a rather complex form of the reduced Liouville equation, see Gotoh & Kraichnan 1993) with the Q derived from the mapping closure approximation (Eq. 22). Then, however, the analysis becomes mathematically dense and numerical solutions are probably the best option.

We here revert to a simple heuristic form of mapping closure, taking ξ to be any component of ξ_{ii} and the mapping function $J = J_{ii}$ to be determined by requiring the probability function Q as derived from substituting for $D\xi/Dt$ from the reduced Eq. 23 into the reduced Liouville equation,

$$\frac{\partial Q}{\partial t} + \frac{\partial}{\partial \xi}\left(\left[\frac{D\xi}{Dt}\right]_{c:u,\xi} Q\right) = \xi Q, \tag{24}$$

(where $[..]_{c:u,\xi}$ denotes the ensemble mean conditional on given values of u and ξ) to be equal to the Q derived from the equivalent for mapping closure (see Gotoh & Kraichnan 1993),

$$\frac{\partial Q(\xi,t)}{\partial t} + \frac{\partial}{\partial \xi}\left(\frac{\partial Y(\xi_o,t)}{\partial t} Q(\xi,t)\right) = \gamma Q(\xi,t), \tag{25}$$

where $\gamma = (\partial/\partial t)\, ln(N/J)$. After some manipulation, this yields an equation for the evolution of J of the form (see also Eq. 24 of Gotoh & Kraichnan (1993))

$$\frac{\partial J}{\partial t} = -r\xi_o J^2 - \mu k_d^2 J^3 + D(J^3) \tag{26}$$

where $k_d^2 = \langle(\partial\xi_o/\partial z)^2\rangle/\langle\xi_o^2\rangle$, angled brackets denoting the ensemble mean and $D(J^3)$ is a function consisting of further non-linear derivative terms of the form J^3. Also, an integral term involving Q is neglected here, which *a posteriori* limits the solutions to high jump Mach numbers $|\xi| > r^2\chi_o$ (χ_o being defined below)

Note that the left hand side and the first two terms on the right are close to the Navier-Stokes form given by Kraichnan (1990), with the addition of the function $r = r_i$ which accounts for compressibility. These terms provide the statistics of the field through a non-linear transformation of the initial field with known statistics. The final term combines together non-linear derivatives, a step which permits further manipulation but with the loss of information concerning the constants of integration.

The evolution of J begins rapidly by the steepening of large velocity gradients (first term on the right), until balance with the viscous term (second term on the right hand side) is achieved. Equating these two terms yields the form of the mapping function: $J = -r\xi_o/(\mu k_d^2)$. Substitution into Eq. 21 yields $\xi = -r^2(t){\xi_o}^2/(\mu k_d^2)$. We convert the initial Gaussian PDF $Q_o(\xi_o)$ into $Q_1(\xi_1)$ by using Eq. 22 to yield the result that the velocity gradient PDF is transformed into an exponential function:

$$Q_1(\xi_1) = \left(\frac{\langle\xi_o^2\rangle}{8\pi r^2\chi_o^2}\right)^{\frac{1}{2}} \frac{N(t)}{|\xi_1|} \exp\left[-\frac{|\xi_1|}{2r^2\chi_o}\right] \tag{27}$$

where $\chi_o = \langle\xi_o^2\rangle/(\nu k_d^2)$. This function has been derived for the high gradients i.e. the shocks, consistent with the numerical simulations.

The exponential being set up, the gradients are then determined by the inviscid terms. Thus, the continued evolution of J is described by the first two terms in Eq. 26 which, on substituting the mapping $J = \xi/(r\xi_1)$ yield

$$\frac{\partial}{\partial t}\left(\frac{\xi/\xi_1}{r}\right) = \xi_1 \frac{(\xi/\xi_1)^2}{r}. \tag{28}$$

This has an asymptotic power law solution of the form $\xi/\xi_1 = 1/(1+t/(t_1))$, t_1 being a constant. Hence, at large t, the velocity gradient associated with a fluid trajectory is inversely proportional to time, as physically plausible for a high Mach number expanding flow. Substituting $\xi_1 = (1 + t/t_1)\xi$ for ξ_1 in Eq. 27, and normalising the PDF through N, yields

$$Q(\xi) = k\frac{\xi_o}{\xi}\exp\left[-\frac{\xi t}{\chi\xi_o t_o}\right]. \tag{29}$$

for large t, where $\chi = 2\, r_o^2\langle\xi_o^2\rangle/(\mu k_d^2\xi_o)$ and k is a constant. Hence, mapping closure predicts, for zero-pressure hydrodynamic flow, the same fast shock decay law as uncovered in the hypersonic simulations.

The above mapping closure technique provides insight into the rapid build up of velocity gradients and transformation to an exponential, as well as the evolution of the exponential term. The form of the prefactor excludes an extension to low speeds.

6.4. A direct physical model

The interpretation we now present is an extension of the dynamic basis of the mapping closure model. First, we neglect viscosity since the long term evolution must be derivable from purely inviscid theory. The critical addition to the above analysis is a result of the simulations: the total number of zones across which the gas is converging remains at approximately 30%, independent of time. This can also be derived from integrating Eqs. (2) and (4) over M_j which yields constant total shock surfaces of $1.05\,10^6$ and $0.10\,10^6$ zone surface elements, respectively (the difference being mainly the factor of 8 more zones in the former 256^3 calculation). As can be seen from Fig. 3), the strong shocks disappear, being replaced by weak shocks. We interpret this empirical conservation law as due to the fluid being contained predominantly within the layers which drive the shocks and the looser-defined layers which drive the weaker compressional waves. These layers interact, *conserving the total shock*

area. This is expected from shock theory since the two driving layers merge but the leading shock waves are both transmitted or reflected. The need for layers to drive the shocks, as opposed to shocks to sweep up the layers, is a necessity in an isothermal flow where the pressure behind a shock must be associated with enhanced density. Nevertheless, a shock will sweep up and compress pre-existing density structures ahead of it.

The decay of a single shock is controlled by the decay of the momentum of the driving layer. The decay of a driving layer is here modelled as due to the time-averaged interaction with numerous other layers. These layers can be represented by an 'ensemble mean' with the average density ρ. Thus a shock is decelerated by the thrust of other shock layers, but its mass is not altered. Mass is not accumulated from the oncoming shock layer, but instead remains associated with the oncoming layer. Then, a layer of column density Σ will experience a deceleration of Σdu/dt = -$C_d\rho$u^2 where C_d is a drag coefficient of order unity and u is the velocity jump (i.e the relative velocity of the layer). Integration yields the result ut/L $\sim \Sigma/(\mathrm{L}\rho)$ for times exceeding Σ/ρu$_o$ where u$_o$ is the initial layer speed.

We impose three physical conditions on the shock distribution.

- At high speeds we take a standard decay law for a number of independently-decaying layers. The decay rate of fast shocks is proportional to the number of shocks present. In this regime, significant numbers of new shocks are not generated.
- Secondly, we shall require that the *total* number of shocks (plus compressional waves, since there is no dividing line in the numerical simulations) remains constant. The function which satisfies both these conditions clearly obeys, on integrating over all shocks with speed exceeding v_1,

$$\frac{d}{dt}\int_{v_1}^{\infty}\frac{dN}{dv}dv = -\kappa(v_1)\int_{v_1}^{\infty}\frac{dN}{dv}dv \tag{30}$$

  with the decay rate function $\kappa(v) \rightarrow 0$ as $v \rightarrow 0$, to conserve the shock number. This has solutions

$$\frac{dN}{dv} = a\,t\frac{d\kappa}{dv}e^{-\kappa t}. \tag{31}$$

  where a is a constant.
- The third condition we invoke is based on the above functional form for individual shock deceleration for which vt is a constant. Then, the number of shocks above any $v = v_o(t_o/t)$ should be conserved i.e.

$$\int_{v_o(t_o/t)}^{\infty}\frac{dN}{dv}dv = constant. \tag{32}$$

  This is similar to the result obtained for the velocity gradients in the mapping closure analysis. Integrating Eq. 30 with this condition then yields the jump distribution function

$$\frac{dN}{dv} = \frac{N_o}{L_o}te^{-vt/L_o}, \tag{33}$$

  where N_o and L_o are constants.

This implies that we have only two constants with which to fit, not a single line, but a whole family of lines! Yet, remarkably, this is quite well achieved, as shown in Fig. 3. Note that the exponential time-dependence is indeed correct at high speeds, but there is a linear time-dependence at low speeds, where the weak shocks accumulate.

6.5. The MHD connection

We have shown that the decaying MHD turbulence with M = 5 possesses similar decay properties to the M = 5 hydrodynamic case despite the different wave phenomena involved. Slow shocks, however, possibly dominate the energy dissipation in the high-field A=1 case. The power is dissipated within shock jumps with Mach numbers in the range $M_j \sim 1-2$. Alfvén waves are an important ingredient in the exponential tail of the velocity jumps. In a uniform medium, Alfvén waves do not decay even when they posess non-linear amplitudes. However, the Alfvén waves in a turbulent medium will interact non-linearly with other Alfvén waves, slow shocks, and density structures. Each Alfvén wave moves through a mean field of other waves. Similarly, each shock layer propagates through the 'mean field' of other shocked layers, the basis utilised in the above physical model for the hydrodynamic case. Hence, the MHD wave interactions could well lead to the decay of the velocity jump distribution in the same manner as shocks.

7. Conclusions

Diffuse gas under various guises is subject to supersonic turbulence. Large-scale numerical simulations of 3D MHD now allow us to explore many variants. Here, we have studied an isothermal gas in which large-scale Gaussian velocity perturbations are introduced and freely decay within a 'periodic box'. Our main aim here is to analyse the distribution of shocks, with the ensuing aim of determining the observational signatures. For this purpose, we have supplemented the original RMS Mach 5 simulations (Mac Low et al. 1998) with hypersonic Mach 50 runs. Indeed, we find that the hypersonic case leads to simple mathematical descriptions for the shock distribution function, from which the M = 5 runs deviate moderately. The Mach 50 runs obey a steeper energy decay law and (hence) have a faster decay of the spectrum of shocks. The velocity PDFs remain near-Gaussian but with increasing asymmetry at higher speeds and lower masses.

It should be remarked that the velocity PDFs distribution and shock distributions decay at different rates. The mass fraction at high speeds decreases faster than the number of shocks with similar speeds. This indicates that the turbulence is indeed decaying from its fully-developed state, and the individual shock structures interfere less with each other as the flow evolves. That is, the saw teeth tend to become more regular with time.

Further conclusions are as follows.

- The magnetic field tends to slow down the spectral decay as well as the overall energy decay. Fast shocks survive longer.

– Transverse waves of a given strength decay faster than waves travelling parallel to the magnetic field.
– Apart from a small initial period, the energy is not dissipated by the fast shocks but by the moderate shocks with jumps in the Mach number from upstream to downstream approximately in the range $M_j = 1 - 3$, even in the M = 50 simulation. This is due to the exponential fall in fast shock numbers, combined with the relatively ineffective dissipation in the weakest shocks.

Our studies show that for hydrodynamic models the ratio of H_ν to dE_{kin}/dt stays at about 65 percent through time, but this ratio varies more with time and has a mean value of 30 percent for MHD models. We conclude that short wavelength MHD waves are present, and energy loss is distributed rather than occuring primarily in thin layers.

In the hypersonic case, we have found simple laws for the evolution and velocity distribution of shock speeds. The same basic exponential spectra are also found for the very closely related high negative velocity gradients of Navier-Stokes and Burgers turbulence, in both simulations and analytical theory (e.g. Kraichnan 1990; Gotoh & Kraichnan 1993). We have extended their heuristic mapping closure model to the present case to reproduce our computed spectral forms, and thus demonstrated some of the dynamical properties which are inherent to supersonic turbulence.

The relevance of studies of decaying supersonic turbulence to star-forming clouds was questioned by Mac Low et al. (1999). The rapid decay implies that such turbulence would be hard to catch in action within long-lived molecular clouds. Possible sites, however, within which decaying turbulence should prove relevant include the regions downstream of bow shocks, clouds suffering a recent impact and disrupted jets. An exponential distribution of shocks such as we find will generate very low excitation atomic and molecular spectra and inefficient electron scattering, leading to steep synchrotron spectra.

In a following paper, these shock spectra will be employed to calculate emission line spectra. On comparison with driven turbulence, we may then begin to understand the type of turbulence we observe and what may be producing the turbulence.

Acknowledgements. MDS benefitted greatly from the hospitality of the Max-Planck-Institut für Astronomie. We thank E. Zweibel for advice and discussions. Computations were performed at the MPG Rechenzentrum Garching. JMZ thanks the American Museum of Natural History for hospitality. Partial support for this research was provided by the US National Science Foundation under grant AST-9800616.

References

Evans C., Hawley J.F., 1988, ApJ 332, 659
Falgarone E., Lis D.C., Phillips T.G., et al., 1994, ApJ 436, 728
Franco J., Carraminana A., 1999, Interstellar Turbulence. CUP, Cambridge
Galtier S., Politano H., Pouquet A., 1997, Phys. Rev. Lett. 79, 2807
Gotoh T., Kraichnan R.H., 1993, Phys. Fluids A 5, 445
Hawley J.F., Stone J.M., 1995, Comp. Phys. Comm. 89, 127
Kraichnan R.H., 1990, Phys. Rev Lett. 65, 575
Lesieur M., 1997, Turbulence in Fluids. Kluwer, Dordrecht
Mac Low M.-M., 1999, ApJ 524, 169
Mac Low M.-M., Ossenkopf V., 2000, A&A 353, 339
Mac Low M.-M., Burkert A., Klessen R., Smith M.D., 1998, Phys. Rev. Lett. 80, 2754
Mac Low M.-M., Smith M.D., Klessen R., Burkert A., 1999, Ap&SS 246, 195
Padoan P., Juvela M., Bally J., Nordlund A., 1998, ApJ 504, 300
Porter D.H., Pouquet A., Woodward P.R., 1994, Phys. Fluids 6, 2133
Smith M.D., Eislöffel J., Davis C.J., 1998, MNRAS 297, 687
Stone J.M., Norman M.L., 1992a, ApJS 80, 753
Stone J.M., Norman M.L., 1992b, ApJS 80, 791
Stone J.M., Ostriker E.C., Gammie C.F., 1998, ApJ 508, 99
Vázquez-Semadeni E., 1994, ApJ 423, 681
Vázquez-Semadeni E., Passot T., Pouquet A., 1996, ApJ 473, 881
von Neumann J., Richtmyer R.D., 1950, J. Appl. Phys. 21, 232